

# In vivo $^{13}\text{C}$ MRS in the mouse brain at 14.1 Tesla and metabolic flux quantification under infusion of [1,6- $^{13}\text{C}_2$ ]glucose

Marta Lai<sup>1</sup>, Bernard Lanz<sup>1</sup>, Carole Poitry-Yamate<sup>2</sup>,  
Jackeline F Romero<sup>2</sup>, Corina M Berset<sup>2</sup>, Cristina Cudalbu<sup>2</sup>  
and Rolf Gruetter<sup>1,2,3,4</sup>

Journal of Cerebral Blood Flow & Metabolism  
2018, Vol. 38(10) 1701–1714  
© Author(s) 2017  
Article reuse guidelines:  
sagepub.com/journals-permissions  
DOI: 10.1177/0271678X17734101  
journals.sagepub.com/home/jcbfm



## Abstract

In vivo  $^{13}\text{C}$  magnetic resonance spectroscopy (MRS) enables the investigation of cerebral metabolic compartmentation while, e.g. infusing  $^{13}\text{C}$ -labeled glucose. Metabolic flux analysis of  $^{13}\text{C}$  turnover previously yielded quantitative information of glutamate and glutamine metabolism in humans and rats, while the application to in vivo mouse brain remains exceedingly challenging. In the present study,  $^{13}\text{C}$  direct detection at 14.1 T provided highly resolved in vivo spectra of the mouse brain while infusing [1,6- $^{13}\text{C}_2$ ]glucose for up to 5 h.  $^{13}\text{C}$  incorporation to glutamate and glutamine C4, C3, and C2 and aspartate C3 were detected dynamically and fitted to a two-compartment model: flux estimation of neuronal metabolism included tricarboxylic acid cycle (TCA) flux in astrocytes ( $V_g = 0.16 \pm 0.03 \mu\text{mol/g/min}$ ) and neurons ( $V_{\text{TCA}}^n = 0.56 \pm 0.03 \mu\text{mol/g/min}$ ), pyruvate carboxylase activity ( $V_{\text{PC}} = 0.041 \pm 0.003 \mu\text{mol/g/min}$ ) and neurotransmission rate ( $V_{\text{NT}} = 0.084 \pm 0.008 \mu\text{mol/g/min}$ ), resulting in a cerebral metabolic rate of glucose ( $\text{CMR}_{\text{glc}}$ ) of  $0.38 \pm 0.02 \mu\text{mol/g/min}$ , in excellent agreement with that determined with concomitant  $^{18}\text{F}$ -fluorodeoxyglucose positron emission tomography ( $^{18}\text{F}$ FDG PET). We conclude that modeling of neuron-glia metabolism in vivo is accessible in the mouse brain from  $^{13}\text{C}$  direct detection with an unprecedented spatial resolution under [1,6- $^{13}\text{C}_2$ ]glucose infusion.

## Keywords

$^{13}\text{C}$  MRS, glucose metabolism, metabolic modelling, mouse brain

Received 27 March 2017; Revised 29 July 2017; Accepted 17 August 2017

## Introduction

$^{13}\text{C}$  magnetic resonance spectroscopy (MRS) is a powerful tool that enables direct measurement of brain metabolic fluxes in vivo in humans and in animal models. The low natural abundance of the  $^{13}\text{C}$  isotope (1.1%) has been exploited by infusing  $^{13}\text{C}$ -labeled substrates, used as tracers, to explore the metabolic fate of the substrate through metabolic pathways of interest by measuring the progressive labeling of the downstream metabolic products. Specifically, given the central role of glucose (Glc) in brain energetics, [1- $^{13}\text{C}$ ]glucose and [1,6- $^{13}\text{C}_2$ ]glucose have been used to assess brain metabolism and neurotransmission mainly through the measurement of the progressive enrichment of glutamate (Glu) and glutamine (Gln) in the positions C4, C3, and C2.<sup>1–3</sup> From the separate

detection of Glu and Gln  $^{13}\text{C}$  peaks, it is possible to assess the rate of the tricarboxylic acid (TCA) cycle, the pyruvate carboxylase pathway (PC), the Glu and Gln cycle through neurotransmission, and the exchange between 2-oxoglutarate (OG) and Glu.

<sup>1</sup>Laboratory for Functional and Metabolic Imaging (LIFMET), École Polytechnique Fédérale de Lausanne, Lausanne, Switzerland

<sup>2</sup>Center for Biomedical Imaging, École Polytechnique Fédérale de Lausanne, Lausanne, Switzerland

<sup>3</sup>Department of Radiology, University of Geneva, Geneva, Switzerland

<sup>4</sup>Department of Radiology, University of Lausanne, Lausanne, Switzerland

## Corresponding author:

Marta Lai, EPFL SB IPHYS LIFMET, CH FI 622 (Bâtiment CH), Station 6, Lausanne CH-1015, Switzerland.  
Email: marta.lai@epfl.ch

Alternatively, brain glucose metabolism can be measured with  $^{18}\text{F}$ -fluorodeoxyglucose positron emission tomography ( $^{18}\text{F}$ FDG PET) allowing the determination of local cerebral metabolic rate of glucose ( $\text{CMR}_{\text{glc}}$ ). The use of  $^{18}\text{F}$ FDG in vivo enables the local estimation of total glucose consumption in oxidative and non-oxidative pathways, however without details on further steps in those biochemical pathways, since it does not provide distinction between different labelled metabolic products (chemical specificity). This extension is made possible when using NMR spectroscopy with introduction of stable isotopes, in particular  $^{13}\text{C}$  MRS.

Although in recent years metabolic modeling of in vivo  $^{13}\text{C}$  MRS data has been successful in describing the compartmentalized metabolism between neuronal and glial cells,<sup>4-8</sup> the applicability of highly detailed models is often limited by the intrinsic low sensitivity of the technique, especially in small volumes, as it is the case for mouse brain. Using direct detection of  $^{13}\text{C}$  nuclei, a large number of  $^{13}\text{C}$  resonances are potentially accessible since the wider chemical shift range associated with  $^{13}\text{C}$  spectra compared to indirect detection via  $^1\text{H}$  nuclei results in well resolved  $^{13}\text{C}$  peaks, however, at the cost of a more significant chemical shift displacement error. Nevertheless, when taking advantage of the smaller  $^1\text{H}$  chemical shift range to perform the localization in the  $^1\text{H}$  channel, detection of broadband localized  $^{13}\text{C}$  MRS in vivo spectra in the rat brain after infusion of  $[1,6-^{13}\text{C}_2]\text{glucose}$  was shown to be feasible at 9.4 Tesla by using  $^1\text{H}$ -localisation and a semi-adiabatic DEPT sequence.<sup>9</sup> Indirect  $^1\text{H}$ - $[^{13}\text{C}]$  MRS detection is an alternative that leads to an increased signal-to-noise ratio (SNR) given the higher gyromagnetic ratio of  $^1\text{H}$ , however at the expense of the smaller  $^1\text{H}$  chemical shift range, which limits the distinct detection of Glu and Gln C3 and especially C2<sup>7,10,11</sup> resonances.

More recently, direct  $^{13}\text{C}$  detection and localization in the  $^1\text{H}$  channel at ultra-high magnetic fields were combined with a neuro-glial modeling scheme<sup>4</sup> leading to an extended characterization of the fluxes related to energy metabolism and neurotransmission between neurons and glia in the rat brain.<sup>6</sup> The separate detection of Glu and Gln at the position C4 and C3 is the minimal prerequisite to distinctly quantify cell-specific, i.e. astrocytes versus neurons metabolism with minimal assumptions, as was earlier shown for  $[1-^{13}\text{C}]$  or  $[1,6-^{13}\text{C}_2]\text{glucose}$  infusion protocols.<sup>12</sup> However, the inclusion of Glu and Gln labeling in the position C2 is typically necessary for two-compartment modelling with minimal a priori constraints on glial TCA cycle ( $V_{\text{g}}$ ) and pyruvate carboxylase rate ( $V_{\text{PC}}$ ) with infused  $^{13}\text{C}$ -labeled glucose. The addition of other time courses such as aspartate (Asp) labelling generally increases the robustness of the model.<sup>6,12</sup> The separate measurement of Asp, Glu and Gln at the position C2 remains only feasible through direct detection due to

the increased spectral dispersion especially at high magnetic fields. The importance of the inclusion of C3 and C2 Glu/Gln time courses in the modeling arises from the influence of  $V_{\text{PC}}$  in their progressive labeling: in fact, this chemical reaction leads to labeling accumulation in the position C2 of Glu and Gln while diluting the positions C3 from the incorporation of a  $^{12}\text{C}$ .

Besides the sensitivity limitation given by the small volume of the mouse brain compared to larger rodents, the experimental protocol brings additional challenges given the difficulty in performing serial blood sampling during the acquisition. Finally, the reduced size of brain structures entails more pronounced magnetic susceptibility variations that will potentially affect the linewidth and consequently the SNR of the spectra. Nonetheless, extending the application of  $^{13}\text{C}$  MRS to the study of mouse brain and eventually applying metabolic modeling could open the way to the characterization of brain metabolism in different animal models within genetically engineered mice.

To our knowledge, in vivo  $^{13}\text{C}$  MRS in the mouse brain was performed only once using direct detection and infusion of  $[1,6-^{13}\text{C}_2]\text{glucose}$ ,<sup>13</sup> however without metabolic modelling interpretation, remaining otherwise mainly limited to rat studies.<sup>5,6,14,15</sup> In the present study, we aimed to combine state of the art techniques in  $^{13}\text{C}$  detection in the mouse brain with metabolic modelling of such data for the quantification of neuro-glial fluxes. High-quality  $^{13}\text{C}$  MRS spectra in volumes as small as 112  $\mu\text{L}$  were needed for the measurement of turnover curves of Glu, Gln and Asp with sufficient temporal resolution to be analyzed with a two-compartment model of brain metabolism accounting for distinct neuronal and astrocytic metabolism.<sup>4</sup> Minimal modelling assumptions resulted in a detailed characterization of mouse brain metabolism. For this purpose, a dedicated high sensitivity  $^{13}\text{C}/^1\text{H}$  surface coil for mice was designed and used in conjunction with a semi-adiabatic polarization transfer sequence to overcome the limitations given by RF field inhomogeneity.  $\text{CMR}_{\text{glc}}$  values derived with PET upon  $^{18}\text{F}$ FDG administration in the same brain region were used to provide a cross-validation of the metabolic flux analysis obtained from  $^{13}\text{C}$  MRS metabolic modeling. The feasibility of detailed in vivo dynamic  $^{13}\text{C}$  MRS in mice potentially opens the way to its applicability to a number of transgenic models available or in smaller brain regions, reaching a new standard in spatial resolution with  $^{13}\text{C}$  direct detection.

## Materials and methods

All animal experimentation procedures were carried out in compliance with the local ethical guidelines (EXANIM, Expérience sur animaux-SCAV, Service

de la consommation et des affaires vétérinaires, Switzerland) and approved by the Veterinary Office of the Canton Vaud. Experimental procedures were reported in compliance with the ARRIVE guidelines.

### *In vivo* $^{13}\text{C}$ NMR spectroscopy

Six male mice (Swiss NUDE, eight weeks old, 28–30 g, Charles River, L'Arbresle Cedex, France) were used for the  $^{13}\text{C}$  MRS experiments. The mice were housed in filter-top cages, with a 12/12-h light-dark cycle, one mouse per cage. Mice were provided with bedding material, enrichment, and nesting material. They were fasted overnight for 7 h with free access to water before studies. Mice were anesthetized with isoflurane (1–1.5%) for tail vein catheter insertion for substrate administration. Respiration rate ( $\sim 100$  bpm) was monitored continuously during mouse anaesthesia (SA Instruments Inc., NY, USA) and isoflurane level adjusted accordingly. After surgical preparation, mice were transferred in the magnet and placed in a home-made holder that allows fixing the head stereotactically with the help of a bite bar/nose cone and ear rods (Rapid Biomedical, Rimpfing, Germany). Body temperature was kept stable (37.0–37.5°C) with the use of a circulating water hose and continuously monitored using a home-built rectal temperature probe. Experiments were performed in a 14.1 Tesla, 26-cm horizontal bore magnet (Varian, Palo Alto, CA/Magnex Scientific, Oxford, UK), using a home-built 9-mm( $^{13}\text{C}$ )/15-mm( $^1\text{H}$  quad) surface coil as receiver and transmitter. The magnet is equipped with actively shielded gradients of (12-cm inner diameter, Magnex Scientific, Oxford, UK) allowing a maximum gradient strength of 400 mT/m in 120  $\mu\text{s}$ . An image acquired with a fast spin-echo sequence was performed in order to position the voxel (TR/TE = 5000/13 ms, FOV = 18  $\times$  18 mm, slice thickness 1 mm, 4 averages). Magnetic field inhomogeneity was minimized by optimizing first and second-order shims with FAST(EST)MAP<sup>16</sup> (21–29 Hz on localized water peak). A  $^1\text{H}$  spectrum was collected in the same voxel as for the dynamic  $^{13}\text{C}$  MRS prior to the adjustment of  $^{13}\text{C}$  MRS parameters and substrate injection, using a short-TE localized SPECIAL sequence<sup>17</sup> (TR/TE = 4000/2.8 ms) in order to obtain total metabolite concentrations. Direct detection was achieved through a semi-adiabatic DEPT polarization transfer sequence (TR = 2.5 s, interpulse delay of 3.8 ms (optimized for  $J_{\text{CH}} = 130$  Hz), 45° for the last  $^1\text{H}$  pulse for the simultaneous detection of CH, CH<sub>2</sub>, CH<sub>3</sub> groups) combined with  $^1\text{H}$  localization.<sup>9</sup> A small sphere filled with 99%  $^{13}\text{C}$ -enriched formic acid was placed on the top of the coil in order to provide a reference signal both for  $^{13}\text{C}$  offset frequency and B<sub>1</sub> calibration in the  $^{13}\text{C}$  channel,

taking into account the changes in coil loading and distance from the measured voxel to the coil. After the calibration, the infusion protocol started with an initial 5-min exponential bolus of 99% enriched [1,6- $^{13}\text{C}_2$ ]glucose, followed by 5 h of continuous infusion of 70% enriched [1,6- $^{13}\text{C}_2$ ]glucose (20% mass per volume solution). The bolus volume per animal weight was 4.01 mL/kg; and the total volume of continuous infusion was 1.99 mL/kg/h. These bolus and continuous infusion rates were established from bench experiments and tail vein blood sampling, where the infusion rate was varied in order to maintain glycemia levels at  $\sim 300$  mg/dL. Localized  $^{13}\text{C}$  spectra were acquired from a volume of 112  $\mu\text{L}$  ( $3.6 \times 6.9 \times 4.5$  mm<sup>3</sup>) covering most of the brain but avoiding lipid contamination from the scalp (Figure 2(c)). Spectra were acquired continuously over 5 h in blocks of 10.6 min. Shimming was repeated every 32 min in order to keep the linewidth constant.

Spectra quantification of  $^1\text{H}$  and  $^{13}\text{C}$  spectra was performed using LCModel.<sup>18</sup> Normalization procedure of spectra for absolute quantification of  $^{13}\text{C}$  metabolite concentrations is described as Supplementary Information. Normalization for RF efficiency on resonances at different frequency offsets as well as for the different efficiency of the DEPT transfer for CH and CH<sub>2</sub> groups was achieved applying a correction factor derived from a natural abundance spectrum acquired on a phantom filled with non-labeled compounds (Glu, Gln, Asp) and scanned under identical experimental conditions.

### $^{18}\text{F}$ FDG positron emission tomography

2-Deoxy-2- $^{18}\text{F}$ -fluoro-D-glucose ( $^{18}\text{F}$ FDG) was delivered to the CIBM from the commercial  $^{18}\text{F}$ FDG production facility at the Center for Radiopharmacy at the University Hospital in Zurich, Switzerland.  $^{18}\text{F}$ FDG was synthesized using aminopolyether supported nucleophilic fluorination of the complex 1,3,4,6-tetra-O-acetyl-2-trifluor-methanesulfonyl- $\beta$ -D-mannopyranose (mannose triflate) as precursor, and the aminopolyether potassium complex [K/2.2.2]<sup>+18F-</sup> as phase-transfer catalyst. This process involved: (a) the addition of mannose triflate into the  $^{18}\text{F}^-$  with acetonitrile; (b) hydrolysis to remove the protective acetyl groups to form  $^{18}\text{F}$ FDG; and (c) purification of the final  $^{18}\text{F}$ FDG product. The injectate was composed by the following components: the active pharmaceutical ingredient  $^{18}\text{F}$ FDG, the nuclide [ $^{18}\text{F}$ ] Fluorine and the pharmaceutical additives: NaH<sub>2</sub>PO<sub>4</sub>·2H<sub>2</sub>O (1.2 mg/ml), Na<sub>2</sub>HPO<sub>4</sub>·2H<sub>2</sub>O (4 mg/ml), NaCl (7.5 mg/ml), and Na<sub>2</sub>S<sub>2</sub>O<sub>3</sub>·5H<sub>2</sub>O (1.3–1.9 mg/ml).

Six healthy male NUDE mice (33.4–35.4 g) were used for the PET experiments. Mice were anesthetized for tail vein catheter insertion (25G home-made

catheter). Initial values of glycemia were obtained at the same time, prior to administration of  $^{18}\text{F}$ FDG. List-mode acquisitions were obtained with a single field of view centered on the body midsection, allowing the inclusion of the brain and inferior vena cava, and initiated with i.v. injection of  $^{18}\text{F}$ FDG ( $1.6 \pm 0.3$  MBq/g body weight; mean  $\pm$  SD; volume of injectate 50–400  $\mu\text{L}$ ) through the tail vein catheter within the first 10 s of the PET scan, followed by 100–150  $\mu\text{L}$  of saline chase solution. Imaging was performed using an avalanche photodiode micro-PET scanner (LabPET4, GammaMedica, Sherbrook Canada). Mice were maintained under 1% isoflurane anaesthesia in oxygen delivered at 0.9 L/min using a face mask with constant monitoring of temperature and breathing rate. An energy window of 250–650 keV and a coincidence timing window of 22.2 ns were used for the detection of photons at 511 keV resulting from annihilated electron-positron pairs. For image reconstruction, a built-in iterative maximum likelihood expectation maximum-based image (MLEM) reconstruction algorithm was used in a cylindrical volume of 46 mm in diameter and 7 cm in length. Voxel size measured  $0.5 \times 0.5 \times 1.18$  mm<sup>3</sup>, giving a typical resolution of <1.2 mm at the center of the FOV.

For temporal histogramming, the following time frames (F) were used: 24 F of 5 s duration; 6 F of 30 s duration; 5 F of 2 min duration; and 7 F of 5 min duration. All post-processing of images was performed using PMOD 2.95 software (PMOD Technologies Ltd, Switzerland).

The image-derived input function (IDIF) was determined from the time activity curves (TAC) of  $^{18}\text{F}$ FDG in the blood at the level of the inferior vena cava.<sup>19</sup> Briefly, the volume of interest (VOI) drawn for the input function consisted in four adjacent regions of interest (1 mm<sup>2</sup> surface and 1.18 mm thickness) in axial slices in correspondence of the vena cava. Their location was established based on visual inspection of the maximum intensity projection image in the coronal plane where the flow of  $^{18}\text{F}$ FDG was observed during the bolus. The brain tissue TACs (tTACs) were selected from mid-brain and were of the same volume and shape as the region scanned during  $^{13}\text{C}$  MRS (Figure 5). The measured radioactivity was corrected for the  $^{18}\text{F}$  radioactive decay (relative to the start of the acquisition).

### Metabolic modeling of $^{13}\text{C}$ MRS data

$^{13}\text{C}$  MRS dynamic data were modelled following a neuro-gliial compartmentalized scheme, as previously shown.<sup>4</sup> Two-compartment scheme for glucose metabolism and label scrambling from [1,6- $^{13}\text{C}_2$ ]glucose into the different carbon positions of the measured amino acids are summarized in Figure 1.

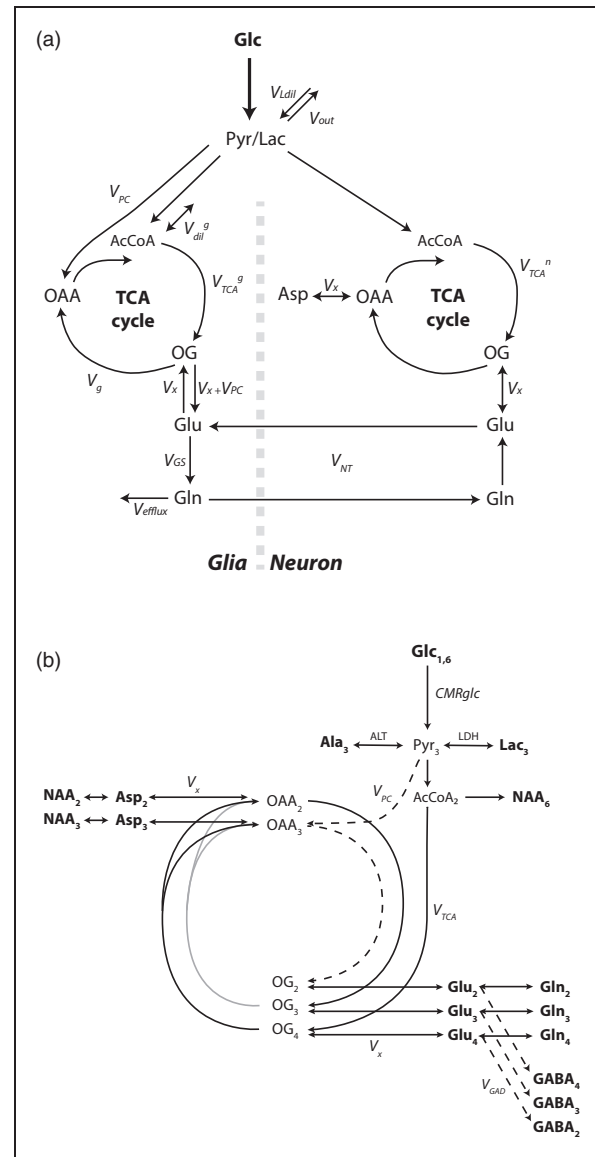


**Figure 1.** (a) Two-compartmental model of neuro-gliial metabolism in the brain used to describe  $^{13}\text{C}$  label transfer upon [1,6- $^{13}\text{C}_2$ ]glucose infusion in the present study. Glucose is rapidly taken up by brain tissue from the blood stream after passing through the blood–brain barrier. Glycolysis converts it into pyruvate (Pyr) which is not detectable *in vivo* due to its small pool size. Given the rapid exchange between Pyr and lactate (Lac) as compared to the TCA cycle flux, they are considered as an indistinguishable pool that is in turn diluted by  $V_{Ldil}$  (inflow from blood-borne lactate) and loses  $^{13}\text{C}$  label through  $V_{out}$  (outflow towards blood). In both compartments, Pyr is converted into acetyl-CoA (AcCoA), which is entering the TCA cycle. The glial compartment is characterized by conversion of Pyr into oxaloacetate (OAA) through pyruvate carboxylase ( $V_{PC}$ ) and by glial specific substrates  $V_{dil}^g$ . Conversion of AcCoA in 2-oxoglutarate (OG) leads to glutamate (Glu) synthesis in both compartments through the trans-mitochondrial flux  $V_x$  ( $V_x + V_{PC}$  in the glial compartment). After a synaptic neurotransmitter release, Glu is rapidly taken up from the synaptic cleft by glial

The two-compartment scheme considers glucose as the main brain energy substrate, where it is rapidly transported from the blood stream through the blood–brain barrier (BBB) into the cerebral tissue compartment. There, glycolysis metabolizes glucose into pyruvate (Pyr) which is, in turn, in rapid exchange with the lactate (Lac) pool through lactate dehydrogenase (LDH) thereby converting labeling in C1 and C6 positions of glucose into C3 of Pyr and lactate.  $^{13}\text{C}$  labeling is diluted at this node due to exchange with blood lactate ( $V_{\text{Ldil}}$ ). Moreover, the model accounts for a small lactate efflux for contribution to non-oxidative pathways ( $V_{\text{out}}$ ). Label from Pyr flows into neuronal and glial TCA cycles: PC activity is essentially localized in the glial compartment<sup>20</sup> contributing to the replenishment of TCA cycle intermediates, while influx of glial-specific substrates is considered through a dilution flux at the level of Acetyl-CoA (AcCoA) in the glial compartment<sup>6</sup> ( $V_{\text{dil}}^{\text{g}}$ ). Label at the level of AcCoA flows through the TCA cycle to 2OG that is in

exchange across the mitochondrial membrane with Glu in both compartments. In the further part of the TCA cycle,  $^{13}\text{C}$  can flow alternatively from OG to oxaloacetate (OAA) for further cycling. The glial TCA cycle flux  $V_{\text{TCA}}^{\text{g}}$  is determined from mass-balance considerations on the OG pool as the sum of the conversion rate between OG and OAA ( $V_{\text{g}}$ ) and  $V_{\text{PC}}$ , while neuronal TCA cycle ( $V_{\text{TCA}}^{\text{n}}$ ) corresponds to Pyr dehydrogenase rate in neurons. In the glial compartment, the forward conversion between OG and Glu occurs at the rate  $V_{\text{x}} + V_{\text{PC}}$ , rather than  $V_{\text{x}}$  solely, due to mass-balance considerations on the TCA intermediate pools. Glu synthesized in neurons is retained in pre-synaptic vesicles, released in the synaptic cleft during the glutamatergic neurotransmission process and promptly taken-up by glial cells after postsynaptic excitation to regulate extracellular Glu homeostasis. Gln synthetase ( $V_{\text{GS}}$ ) synthetizes Gln from Glu specifically in the glial compartment.<sup>21</sup> Again, mass-balance considerations on glial Glu and Gln lead to the equivalence  $V_{\text{GS}} = V_{\text{NT}} + V_{\text{PC}}$  and the correspondence  $V_{\text{efflux}} = V_{\text{PC}}$  at metabolic steady-state. Finally, Gln participates indirectly to neurotransmission by being released in the extracellular space and subsequently taken up by neurons, serving as precursor for Glu synthesis and replenishment of neurotransmitter vesicles. The transmitochondrial flux  $V_{\text{x}}$  acts as exchange flux between OAA and Asp pools as well as between OG and Glu in neurons in the malate-Asp shuttle.

The set of differential equations that characterize the  $^{13}\text{C}$  labelling dynamics in the presented two-compartment model was derived from the reaction pathways in the neuronal and the glial compartments as described above at metabolic steady-state (see Supplementary Information). The input function was generated as a step function with 70% glucose fractional enrichment (FE).

$^{13}\text{C}$  time courses obtained from spectral quantification of individual animals were first averaged over all the subjects. The values of the metabolic fluxes characterizing the two-compartment model ( $V_{\text{tca}}^{\text{n}}$ ,  $V_{\text{g}}$ ,  $V_{\text{x}}$ ,  $V_{\text{PC}}$ ,  $V_{\text{NT}}$ ,  $V_{\text{dil}}^{\text{g}}$ , and  $V_{\text{out}}$ ) were determined in a two-step process. First, the set of differential equations was at first iteratively solved with a Runge–Kutta method and solutions were fitted to the measured  $^{13}\text{C}$  FE turnover curves by adjusting the metabolic flux values (regression parameters) using a Levenberg–Marquardt algorithm for non-linear regression. FE curves were weighted in the regression cost function by the inverse of their variance, based on their respective noise level, to avoid bias in the parameters regression. In the second step, the precision of the estimated fluxes was determined by Monte Carlo (MC) simulation of the  $^{13}\text{C}$  FE time courses ( $N = 300$ ).<sup>22</sup> Briefly, after the estimation of the metabolic fluxes by the weighted regression

#### Figure 1. Continued

cells at an apparent neurotransmission rate ( $V_{\text{NT}}$ ), converted into glutamine (Gln) through the action of glutamine synthetase ( $V_{\text{GS}}$ ) and released in the extracellular space where it is mainly taken back by neurons for conversion into Glu and refilling of the neurotransmitter vesicles, completing the Glu/Gln cycle. Alternatively, Gln is released in the extracellular space generating a net efflux ( $V_{\text{efflux}}$ ) which is compensated by de novo biosynthesis of TCA cycle intermediates in the glial compartment through  $V_{\text{PC}}$ . Aspartate (Asp) labeling is essentially attributed to the neuronal compartment from the direct exchange with OAA through  $V_{\text{x}}$  in the malate/aspartate shuttle. (b)  $^{13}\text{C}$  labeling scheme from [1,6- $^{13}\text{C}_2$ ]glucose ( $\text{Glc}_{1,6}$ ) metabolism through glycolysis and TCA cycle. Metabolites visible at steady-state in typical in vivo scans are marked in bold.  $\text{Glc}_{1,6}$  leads to C3 labeling in pyruvate ( $\text{Pyr}_3$ ). Alanine transaminase (ALT) and lactate dehydrogenase (LDH) regulate the labeling transfer to alanine C3 ( $\text{Ala}_3$ ) and lactate C3 ( $\text{Lac}_3$ ), respectively. Alternatively,  $\text{Pyr}_3$  labels the C4 position in 2-oxoglutarate ( $\text{OG}_4$ ) and glutamate ( $\text{Glu}_4$ ) and consequently in glutamine ( $\text{Gln}_4$ ), through the TCA cycle and further through glutamate/glutamine cycling. Multiple turns of the TCA cycle (grey lines) eventually lead to a progressive labeling of the positions C3 and C2 according to the scheme.  $V_{\text{PC}}$  (dashed line) brings additional labeling at the position C2 as well as a dilution at the position C3 of OG, reflected in glutamate and glutamine and representing a distinctive feature for glial compartment TCA metabolism. GABA C4 ( $\text{GABA}_4$ ), C3 ( $\text{GABA}_3$ ), and C2 ( $\text{GABA}_2$ ) are synthetized from glutamate C2 ( $\text{Glu}_2$ ), C3 ( $\text{Glu}_3$ ), and C4 ( $\text{Glu}_4$ ), respectively, through GABAergic neurotransmission ( $V_{\text{GAD}}$ ). The transmitochondrial flux  $V_{\text{x}}$  regulates the exchange between oxaloacetate and aspartate that will in turn label N-acetyl aspartate (NAA). Only the positions C2 and C3 of aspartate ( $\text{Asp}_2$ ,  $\text{Asp}_3$ ) and NAA ( $\text{NAA}_2$ ,  $\text{NAA}_3$ ) are visible in the observed chemical shift range. NAA is also labeled at the position C6 ( $\text{NAA}_6$ ) from acetyl-CoA ( $\text{AcCoA}_2$ ).

method, the fluxes were employed to generate a collection of noise-free  $^{13}\text{C}$  FE turnover curves, also used to evaluate the noise level in each turnover curve by subtraction:  $N$  sets of artificial  $^{13}\text{C}$  turnover curves were generated by adding  $N$  realizations of Gaussian noise with corresponding noise level to the noise-free model curves. A probability distribution for each metabolic flux is then obtained by fitting the  $N$  sets of artificial turnover curves. The standard deviation (SD) of each distribution determines the uncertainty on the estimated fluxes.

### Metabolic modeling of $^{18}\text{F}$ FDG kinetics in PET experiments

The time activity curves of  $^{18}\text{F}$ FDG acquired from the blood and the brain over a 50 min duration were processed using Patlak graphical analysis,<sup>23</sup> allowing an estimation of  $\text{CMR}_{\text{glc}}$  from the slope of the resulting linear segment for each animal. The model predicts that for a time  $t > t^*$ , a linear relationship will be established between  $\frac{C_t^*(t)}{C_p^*(t)}$  versus  $\frac{\int_0^t C_p^*(s) ds}{C_p^*(t)}$  where  $C_p^*(t)$  represents the plasma  $^{18}\text{F}$ FDG radioactivity concentration (in kBq/ml) at a given time  $t$ , and  $C_t^*(t)$  the total tissue radioactivity concentration. The slope of the linear fitting curve is equal to  $K^*$  from which  $\text{CMR}_{\text{glc}}$  is estimated as

$$\text{CMR}_{\text{glc}} = \frac{C_p}{LC} K^* \quad (1)$$

where  $C_p$  is the plasma glucose concentration, and  $LC$  is the lumped constant, fixed to 0.625 for mice.<sup>24,25</sup> Plasma glucose is assumed to remain constant throughout the PET scan, which is supported by the fact that  $^{18}\text{F}$ FDG is injected in pM concentrations and it is presumed not to perturb glucose homeostasis.

Biological systems can be studied with a Patlak analysis under the essential condition of irreversible trapping of the tracer under study, meaning that once  $^{18}\text{F}$ FDG is metabolized in the cell (i.e. it undergoes phosphorylation), de-phosphorylation is not possible ( $k_4^* = 0$ ). This assumption can be considered valid for a scanning duration shorter than 27 min in the mouse brain.<sup>25-27</sup> On the other hand, the time point  $t^*$  defines the time delay that is necessary to reach equilibrium in FDG transport that will hence become unidirectional. In the IF,  $t^*$  is the time point characterized by a nearly zero-slope in the curve after the bolus peak. Passed that time, FDG radioactivity concentration in blood will continue to decrease due to a combined effect of FDG uptake by major organs and muscles, as well as kidneys and bladder (frequently referred to as product loss). Specific  $t^*$  of 5 min was chosen to allow sufficient

time for reaching equilibrium in the exchange between plasma and tissue compartment.

The complete equation for the Patlak regression line is

$$\frac{C_t^*(t)}{C_p^*(t)} = K^* \frac{\int_0^t C_p^*(s) ds}{C_p^*(t)} + V_d \quad (2)$$

where  $V_d$  accounts for the non-zero intercept in the  $y$  axis, which represents the initial volume of distribution.

## Results

In vivo  $^{13}\text{C}$  MR spectra were obtained dynamically from mouse brain in six animals for up to 5 h during infusion of  $[1,6-^{13}\text{C}_2]\text{glucose}$ , in a volume of interest of 112  $\mu\text{L}$  (Figure 2(c)).  $^{13}\text{C}$  MRS spectra acquired during the first 2.5 h with a temporal resolution of 10.6 min showed excellent sensitivity and spectral resolution in the selected VOI, reaching an SNR of eight after only 160 min (Figure 2(b)). GlcC6, LacC3 and GluC4 peaks rose in magnitude from the first 5 min, reflecting a prompt increase of blood glucose  $^{13}\text{C}$  level. Other amino acid resonances were increasingly visible during the first hour (Figure 2(a)). Spectral resolution was such that Glu and Gln peaks were well separated in all carbon positions C4, C3, and C2.

Steady-state spectra acquired during 92 min after 3.5 h of  $[1,6-^{13}\text{C}_2]\text{glucose}$  infusion, showed outstanding SNR ( $>20$ ) and spectral resolution (FWHM = 15 Hz) allowing detection of 17 distinct resonances (Figure 3(a)) that account for a wide range of brain metabolites involved in glucose glycolytic catabolism and oxidation, synthesis of aminoacids and neurotransmitters. GlcC6 was the first peak to appear followed by LacC3 (Figure 2(a)), labeled from PyrC3 as AlaC3 (Figure 1(b)). Although cerebral alanine (Ala) has a relatively small pool size compared to Lac, AlaC3 became visible during the first hour (Figure 2(a)) and appeared clearly in steady-state spectra (Figure 3(a)). GABA is the primary neurotransmitter involved in inhibitory signaling and is directly synthesized by GABAergic neurons from Glu. Therefore, label in positions C4, C3, and C2 of Glu is transferred to GABAC2, C3, and C4, respectively, resulting in the appearance of fairly prominent peaks given its relatively large pool size in the striatum ( $3.1 \pm 0.2 \mu\text{mol/g}$ , mean  $\pm$  SD, as measured from the pre-infusion  $^1\text{H}$  MRS scan). Asp is labeled from OAA through the  $V_x$  exchange flux (Figure 1(b)) in its four carbon positions. However, only the C2 and C3 positions, namely at 53.2 and 37.4 ppm, fall within the detectable chemical shift range. Finally, Asp acts as a precursor for NAA labeling in C2 and C3, while the C2 carbon of AcCoA is the label precursor for NAAC6. NAA peaks in these three

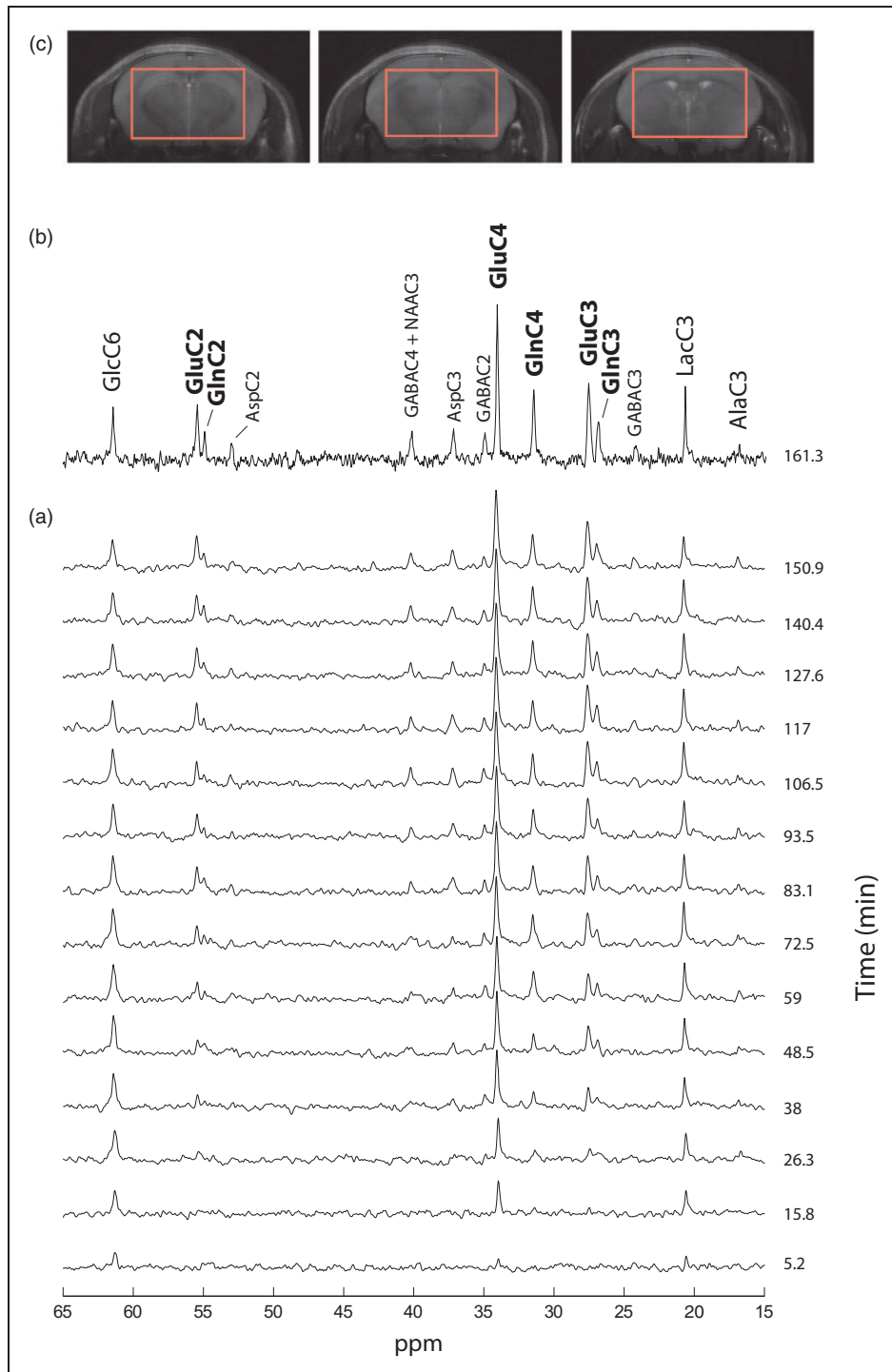


**Figure 2.** Typical  $^{13}\text{C}$  MRS spectra acquired at 14.1 Tesla in a volume of  $112\ \mu\text{L}$  and a time resolution of 10.2 minutes. (a) Spectra collected after the bolus of 99%-enriched  $[1,6\text{-}^{13}\text{C}_2]\text{glucose}$  and during continuous infusion for the first 150 mins with a temporal resolution of 10.2 min. Spectral SNR is enhanced by exponential apodisation ( $l_b = 25\ \text{Hz}$ ). (b) Spectrum acquired at 160 min following the bolus during 10.2 minutes ( $\text{SNR} = 11$ ;  $l_b = 9\ \text{Hz}$ ). (c) Three consecutive coronal slices (1 mm thick) of a T2-weighted image acquired prior to  $^{13}\text{C}$  MRS experiments showing voxel localization in the middle brain ( $3.6 \times 6.9 \times 4.5\ \text{mm}^3$ ).

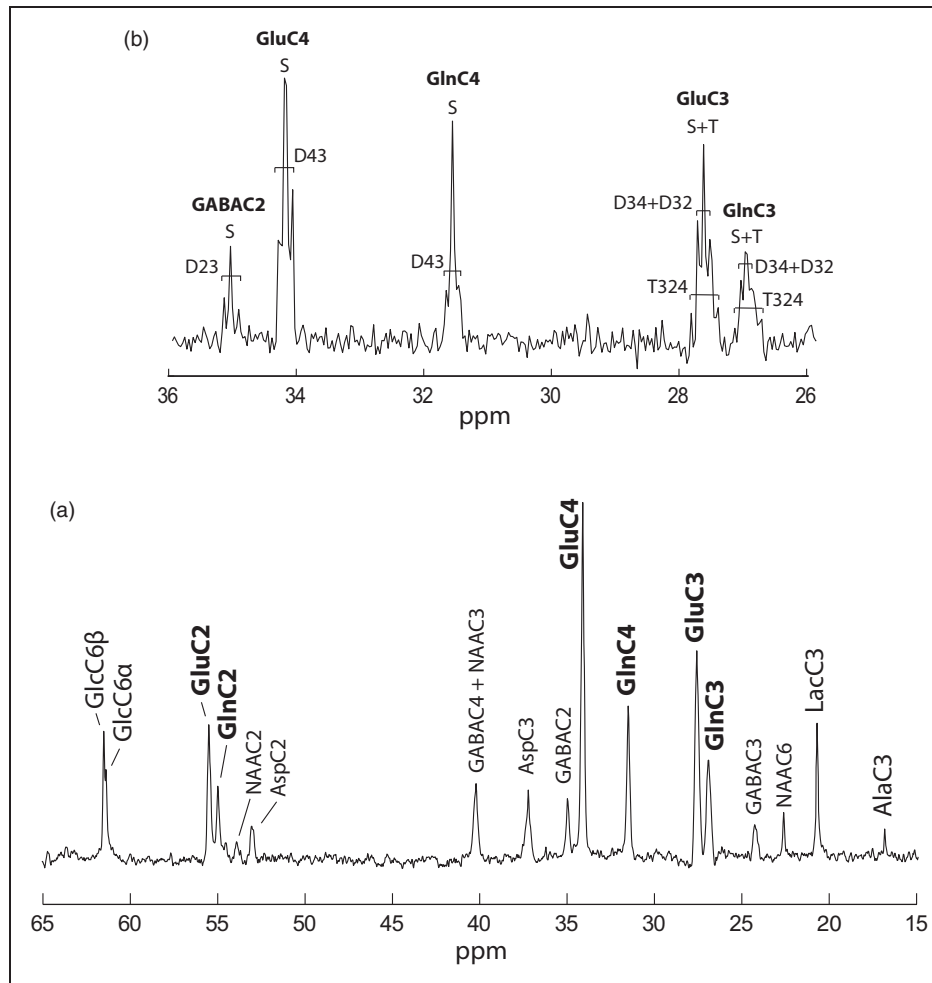


**Figure 3.** (a)  $^{13}\text{C}$  MRS in vivo spectrum representative of typical data acquired at steady state (3.5 h after the bolus; SNR = 24) for 92 min in the selected VOI (Figure 2(c)). (b) Multiplet resolution reached at the positions C4 and C3 of Glu and Gln. Doublet and singlet at the position C2 of GABA are also visible at 35.2 ppm.

positions were clearly detected in steady-state spectra (Figure 3(a)). High spectral resolution allowed distinct detection of multiplets at the position C3 and C4 of Glu and Gln (Figure 3(b)). This feature allowed the calculation of the FE of GluC3 at steady-state and therefore the rescaling of  $^{13}\text{C}$  concentrations in the spectra (see Supplementary Information).

The fairly tight SD of the FE curves (Figure 4) demonstrated high reproducibility between animals. Maximal FE in GluC4 and GlnC4 reached 50% and 37%, respectively, at steady-state, while positions C3 were at 40% and 32%, respectively, indicating that the latter were likely diluted by PC activity. The lower FE of carbons C4 compared to glucose (70%) is the direct consequence of the dilution flux at the level of the lactate pool ( $V_{\text{out}}$ ) which will equally influence Glu and Gln, while incorporation of glial-specific substrates ( $V_{\text{dil}}^{\text{g}}$ ) results mostly in the dilution of Gln

curves. Moreover, PC introduces additional labeling in the positions C2 of Glu and Gln: this was observable from a higher FE of 44% and 41% at steady-state, respectively, compared to the C3 carbons. Experimental curves of Glu C4, C3, and C2, Gln C4, C3, and C2 and AspC3 were fitted by the two-compartmental model for brain metabolism (Figure 1(a)). The following metabolic fluxes were determined (Table 1): neuronal TCA cycle ( $V_{\text{TCA}}^{\text{n}} = 0.56 \pm 0.03 \mu\text{mol/g/min}$ ), glial TCA cycle ( $V_{\text{g}} = 0.16 \pm 0.03 \mu\text{mol/g/min}$ ), PC activity ( $V_{\text{PC}} = 0.041 \pm 0.003 \mu\text{mol/g/min}$ ), mitochondrial flux ( $V_{\text{x}} = 0.18 \pm 0.02 \mu\text{mol/g/min}$ ), apparent neurotransmission ( $V_{\text{NT}} = 0.084 \pm 0.008 \mu\text{mol/g/min}$ ), dilution in the Lac pool ( $V_{\text{out}} = 0.20 \pm 0.02 \mu\text{mol/g/min}$ ) due to non-oxidative utilization of glucose or incorporation of other unlabeled substrates and dilution in the glial pool ( $V_{\text{dil}}^{\text{g}} = 0.23 \pm 0.05 \mu\text{mol/g/min}$ ) due to glial-specific substrates.  $\text{CMR}_{\text{glc(ox)}}$

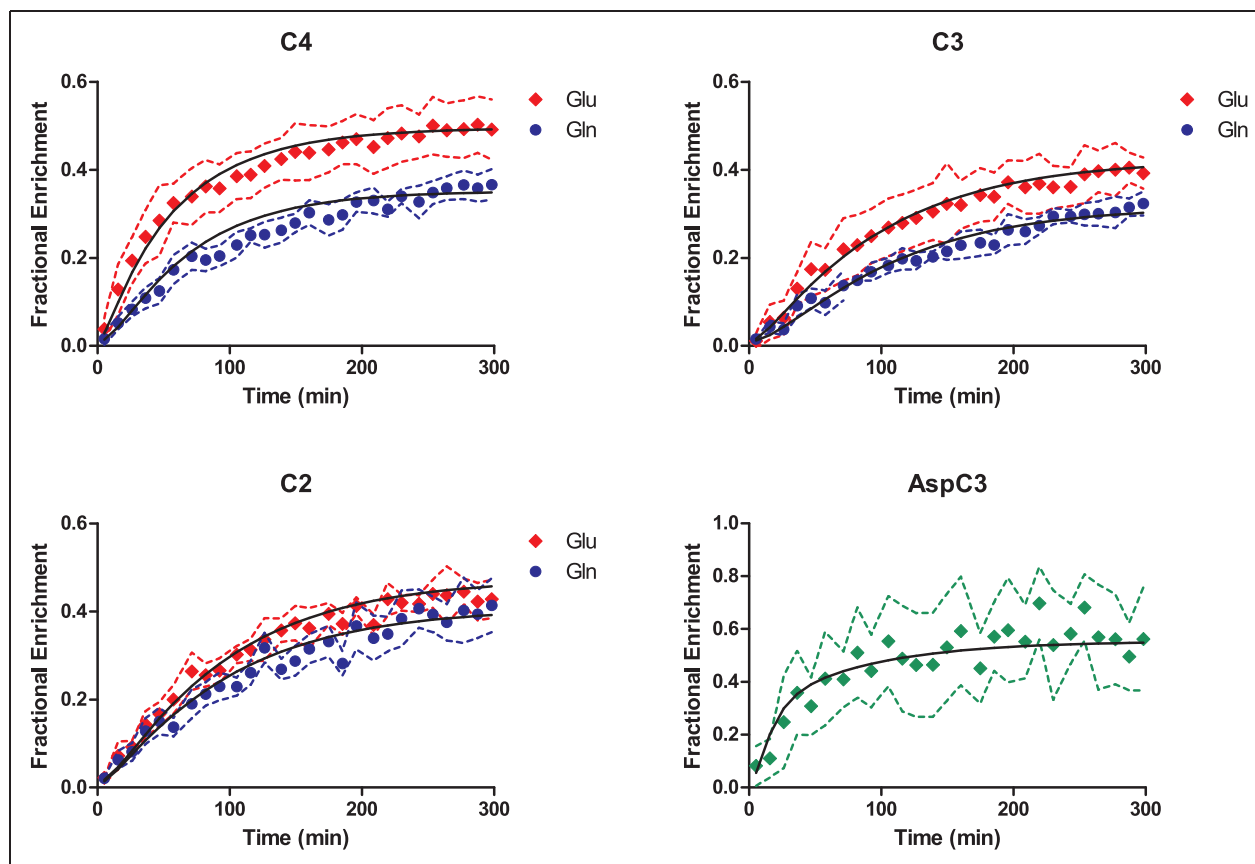


**Figure 4.** Fractional enrichment curves of Glu and Gln at the position C4, C3, and C2 and Asp C3 as fitted to the neuro-glia compartmental model (Figure 1(a)). The black solid line represents the best fit as obtained by least square fitting. Dashed lines represent SD range determined from MC simulation for each experimental curve.

**Table 1.** Metabolic fluxes estimated in the mouse brain in vivo.

Flux	$V_g$	$V_{TCA}^n$	$V_{PC}$	$V_x$	$V_{NT}$	$V_{out}$	$V_{dil}^g$	$CMR_{glc(ox)}$
Mean $\pm$ SD ( $\mu\text{mol/g/min}$ )	$0.16 \pm 0.03$	$0.56 \pm 0.03$	$0.041 \pm 0.003$	$0.18 \pm 0.02$	$0.084 \pm 0.008$	$0.20 \pm 0.02$	$0.23 \pm 0.05$	$0.38 \pm 0.02$

Note: Metabolic fluxes (expressed in  $\mu\text{mol/g/min}$ ) determined from metabolic modeling of experimental data, based on the scheme shown in Figure 1. Errors express SD derived from MC simulation with a set of  $N=300$  artificial set of curves for Glu, Gln, and Asp.  $CMR_{glc(ox)}$  is calculated as  $(V_{TCA}^n + V_{TCA}^g + V_{PC})/2$ .  $V_{TCA}^n$ : rate of neuronal TCA cycle;  $V_g$ : rate of glial TCA cycle;  $V_{PC}$ : pyruvate carboxylase rate;  $V_x$ : transmittochondrial flux rate;  $V_{NT}$ : apparent rate of glutamatergic neurotransmission.

( $0.38 \pm 0.02 \mu\text{mol/g/min}$ ) was determined as  $(V_{TCA}^n + V_{TCA}^g + V_{PC})/2$ .

To determine the total  $CMR_{glc}$  independently from  $^{13}\text{C}$  MRS experiments, we used  $^{18}\text{F}$ FDG PET. Specifically,  $CMR_{glc}$  rates in mice brain were determined by metabolic modeling of  $^{18}\text{F}$ FDG uptake with Patlak graphical analysis, dynamically detected in a group of six mice. Data were quantified in a voxel corresponding to the one used for  $^{13}\text{C}$  MRS located in the mid brain (Figure 5(b)). Examination of linearity in Patlak plots between 5 and 27 min from the injection

led to quantification of  $CMR_{glc}$  for each animal.  $R^2$  values (0.92–0.99) were examined to evaluate the goodness of the fit in the selected time frame. Averaging of  $CMR_{glc}$  over the entire group resulted in a global value of  $0.4 \pm 0.1 \mu\text{mol/g/min}$  (mean  $\pm$  SD).

## Discussion

In the present study, direct detection  $^{13}\text{C}$  MRS spectra were applied from the mouse brain to quantify compartmentalized metabolism between neurons and glial

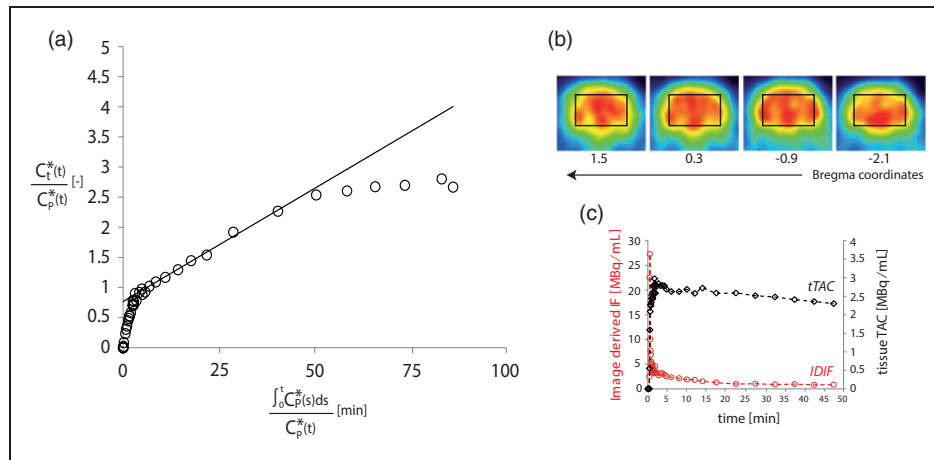


**Figure 5.** (a) Example of Patlak graphical analysis on a single  $^{18}\text{F}$ -FDG PET experiment. Linear fit performed between 5 and 27 min is shown with a solid black line. A significant  $k_4^*$  activity is visible in the last points from a concave inflection of the Patlak plot. (b) Reconstructed PET images from the middle brain showing the respective ROIs in four consecutive coronal slices (reconstructed voxel size  $0.5 \times 0.5 \times 1.18 \text{ mm}^3$ ). (c) Example of  $^{18}\text{F}$ FDG kinetics after the bolus injection: red dots show the image-derived input function (IDIF) determined from the vena cava while black squares correspond to the tissue time activity curve (tTAC) measured in the brain VOI.

cells. Monte Carlo simulation showed that metabolic rates were precisely determined, including the fluxes specific to the glial compartment (maximal error of 19% on  $V_g$ ).

The high spectral quality attained was achieved by integrating state of the art  $^{13}\text{C}$  direct detection<sup>9</sup> and shimming techniques<sup>16</sup> at ultra-high field (14.1 Tesla), combined with the use of an optimized homemade  $^1\text{H}$ - $^{13}\text{C}$  surface coil. The excellent sensitivity achieved in an exceptionally small volume (i.e.  $112 \mu\text{L}$ , Figure 2(c)) allowed separate detection of three aliphatic carbons of Glu and Gln (C4, C3, and C2) up to  $^{13}\text{C}$ - $^{13}\text{C}$  multiplet resolution (Figure 3(b)) as well as the measurement of a wide range of brain metabolites linked to glucose metabolism in the brain, as Asp, GABA, NAA, Ala, and Lac. All peaks were separately resolved (Figure 3(a)) with the only exception of GABAC4 and NAAC3 that have very similar chemical shifts (respectively 40.2 and 40.3 ppm), thus appearing inevitably overlapped, even at this field strength.

Direct detection technique further allowed separate detection of Glu and Gln in the position C2 that are commonly overlapped in indirect  $^1\text{H}$ - $^{13}\text{C}$  MRS detection.<sup>7,10,11,28,29</sup>  $V_{\text{PC}}$  enables de novo synthesis of carbon skeletons entering the TCA cycle specifically in the glial compartment and introduces additional labeling at the level of Gln C2, while diluting the C3 position. Thus, the distinct detection of GlnC2 and GluC2 time courses is of great importance when aiming for robustness in metabolic modeling of neuro-glial interactions with minimal assumptions.<sup>6,12</sup>

The high temporal resolution of the measurements, i.e. 10.6 min (Figure 2), allowed for mathematical modeling of neuro-glial metabolism, based on labelling of Glu and Gln at the carbon positions C4, C3, and C2 and Asp at the position C3. The measurements were assessed to be highly reproducible between individual animals, as seen from the relatively narrow SD intervals of the group-averaged  $^{13}\text{C}$  turnover curves. This was ascribed to the implementation of the standardized infusion protocol and reproducible experimental conditions, despite the inaccessibility of plasma glucose level during infusion.

### Metabolic fluxes

The present study represents to our knowledge the first attempt of mathematical modeling of cerebral metabolism in mice based on in vivo  $^{13}\text{C}$ -labeling experiments with direct  $^{13}\text{C}$  detection. Previous studies<sup>4-6,14,15</sup> have applied similar techniques to the human and rat brain gaining important insights on cerebral metabolic compartmentation, whereas cerebral metabolism in mice has only been described by ex vivo measurements<sup>30</sup> or by  $^{13}\text{C}$  indirect detection<sup>11</sup> subsequently analysed by simplified one-compartment model of brain metabolism. While indirect detection gave access to real-time information on the pool size during infusion,<sup>11</sup> including the input function,<sup>11</sup> direct detection reduces the peak overlap and increases the number of dynamically detectable metabolites carbon positions. In the present model,  $^1\text{H}$  MRS spectra enabled the determination of metabolites pool size in vivo to derive FE values for

**Table 2.** Review of the previously published values of metabolic fluxes ( $\mu\text{mol/g/min} \pm \text{SD}$ ).

Metabolic flux quantification from animal and human $^{13}\text{C}$ MRS experiments in resting brain							
Reference	Species	$V_{\text{TCA}}^{\text{n}}$	$V_{\text{TCA}}$	$V_{\text{g}}$	$V_{\text{x}}$	$V_{\text{NT}}$	$V_{\text{PC}}$
40	Rat	–	$0.46 \pm 0.12$	–	–	–	–
10	Rat	$0.79 \pm 0.15^{\text{a}}$ $0.20 \pm 0.11^{\text{b}}$	–	$5\% V_{\text{TCA}}^{\text{n c}}$	$12.4 \pm 4.5^{\text{b}}$ $6.1 \pm 3.3^{\text{c}}$	$0.31 \pm 0.07^{\text{a}}$ $0.02 \pm 0.04^{\text{b}}$	$0.096^{\text{c}}$
6	Rat	$0.46 \pm 0.01$	–	$0.21 \pm 0.02$	$0.99 \pm 0.12^{\text{d}}$	$0.10 \pm 0.01$	$0.067 \pm 0.004$
8	Rat	$0.37 \pm 0.06$	–	$0.27 \pm 0.02$	$0.46 \pm 0.05^{\text{d}}$	$0.15 \pm 0.01$	$0.087 \pm 0.012$
2,e	Human	$0.70 \pm 0.09$	$0.69 \pm 0.06$	$0.09 \pm 0.04$	–	$0.26 \pm 0.08$	$0.06 \pm 0.03$
11	Mouse <sup>f</sup>	–	$1.05 \pm 0.04$	–	$0.48 \pm 0.02$	$0.20 \pm 0.02$	–
30	Mouse <sup>g</sup>	$0.75 \pm 0.05$	$0.83 \pm 0.07$	$0.02 \pm 0.04$	$99.96^{\text{h}}$	$0.18 \pm 0.01$	$0.06 \pm 0.03$

<sup>a</sup>Grey matter, glial TCA cycle fixed at  $5\%V_{\text{TCA}}^{\text{n}}$ ,  $V_{\text{PC}}$  fixed at  $0.096 \mu\text{mol/g/min}$ .

<sup>b</sup>White matter, glial TCA cycle fixed at  $5\%V_{\text{TCA}}^{\text{n}}$ ,  $V_{\text{PC}}$  fixed at  $0.096 \mu\text{mol/g/min}$ .

<sup>c</sup>Fixed values or modeling constraint.

<sup>d</sup>Transmitochondrial flux between 2OG and Glu in neurons.

<sup>e</sup>Mean and SD from published results in  $^{13}\text{C}$  MRS experiment in resting awake human subjects in midline occipital/parietal lobe.

<sup>f</sup>Spectra acquired in the cortex and striatum,  $V_{\text{NT}}$  was set to exchange rate between Glu and Gln ( $V_{\text{gln}}$ ).

<sup>g</sup>Analysis of brain extracts from the striatum; three-compartment model is assumed, distinguishing between GABAergic and glutamatergic neurotransmission ( $V_{\text{NT}}$  refers to glutamatergic neurotransmission).

<sup>h</sup>Iterated values in the modeling procedure.

Note: Fluxes are quantified from  $^{13}\text{C}$  in vivo experiments in humans, monkeys, rats, and mice. Since available published metabolic fluxes quantified in vivo in mice are limited, values from mice extracts were included.<sup>30</sup> Results are derived from the whole brain if not stated otherwise.

TCA: tricarboxylic acid;  $V_{\text{TCA}}^{\text{n}}$ : rate of neuronal TCA cycle;  $V_{\text{TCA}} = V_{\text{TCA}}^{\text{n}} + V_{\text{g}} + V_{\text{PC}}$ : average of TCA cycle rates among neurons and glia;  $V_{\text{g}}$ : rate of glial TCA cycle;  $V_{\text{PC}}$ : pyruvate carboxylase rate;  $V_{\text{x}}$ : transmitochondrial flux rate;  $V_{\text{NT}}$ : apparent rate of glutamatergic neurotransmission.

each metabolite included in the metabolic modeling, by assuming constant pool size over the experiment.

The obtained neuronal and glial TCA cycle fluxes were comparable with values from published data in human and rat brain in vivo as well in the mouse brain ex vivo (Table 2). Neuronal TCA cycle rate in the awake human brain at rest averages to  $0.7 \pm 0.09 \mu\text{mol/g/min}^2$ , while it tends to be lower in rats and mice (Table 2).

The transmitochondrial exchange flux  $V_{\text{x}}$  was comparable to  $V_{\text{TCA}}^{\text{n}}$ , similar to previous studies.<sup>3,11,6,15,31</sup> This implies that the malate-Asp shuttle is a major mechanism of label transfer across the mitochondrial membrane, as discussed previously.<sup>3</sup>

The metabolic fluxes determined in this study represent an average over the examined VOI and are thus expected to be mostly influenced by metabolic exchanges in the central part of the brain, mainly the striatum.  $V_{\text{NT}}$  can vary considerably through different brain regions and is typically higher in regions dominated by excitatory synapses (i.e. cortex) characterized by higher rates of glucose oxidation.<sup>30</sup> Conversely, the striatum is known for the higher level of GABA (and therefore likely higher role of GABAergic neurotransmission) when compared to cortex, hippocampus and cerebellum<sup>30,32</sup> and the lower rate of excitatory neurotransmission compared to other regions in the mouse brain.<sup>30</sup> Therefore, the rate  $V_{\text{NT}}$  found in this study reflected this pattern and

was consistent with previously published values in rats in vivo.<sup>8,6</sup> Glial TCA cycle rate and PC rate were in agreement with previously published values in rats (Tables 1 and 2), with  $V_{\text{PC}}$  being one order of magnitude smaller than  $V_{\text{g}}$ .

Beyond these observations, metabolic rates could be dependent on the specific strain used in the experiment and possibly from the use of anaesthetics.<sup>33,34</sup> However, a deeper understanding of these aspects is far from being attained given the limited number of studies available on the topic.

In our study, the levels of brain Lac ( $4.3 \pm 0.8 \mu\text{mol/g}$ ), enabled the measurement of Lac enrichment turnover, as early as 5 min after the start of the infusion.  $^1\text{H}$  MRS studies of metabolite concentrations in the mouse brain indicated a higher cerebral Lac concentration in this species<sup>32</sup> compared to rats,<sup>35</sup> especially in the striatum, where levels as high as  $5 \mu\text{mol/g}$  were reported in C57BL/6 mice.<sup>32</sup> Given this relatively low concentration in rats (usually below  $2 \mu\text{mol/g}$  in the rat striatum<sup>35</sup>), Lac peaks are often barely detectable in  $^{13}\text{C}$  MRS studies under physiological conditions upon infusion of labeled glucose,<sup>9,6</sup> whereas a complete time course was registered in the mouse brain by  $^{13}\text{C}$  indirect detection.<sup>11</sup> Therefore, in such experiments, which give access to dynamic information of the Lac pool size, the  $^{13}\text{C}$  Lac signal could in principle be used as input function of the mathematical modeling, as previously demonstrated<sup>11</sup>. However, in  $^{13}\text{C}$  direct detection

studies, it is generally not recommended to determine dynamically the Lac FE curve by assuming a constant pool size for Lac, since volatile anaesthetics<sup>36,37</sup> and nearly hyperglycemic plasma concentrations of glucose could induce fluctuations of total Lac concentration over the course of the experiment and would similarly influence Ala. Increasing pool size of the measured metabolites does not represent an obstacle to the measurement of metabolic fluxes, as non-steady-state regime can be taken into account in the modeling when real-time information on metabolite pool size is accessible.<sup>8,11</sup>

### *CMR<sub>glc</sub> determined by <sup>18</sup>FDG PET experiments*

Total cerebral glucose consumption was evaluated by simplified <sup>18</sup>FDG kinetic modeling: the linear regression method applied in Patlak plots for each animal enabled the determination of the CMR<sub>glc</sub> in the VOI matched to that of <sup>13</sup>C MRS, under the fundamental assumption of irreversible FDG-6P kinetics. Patlak graphical analysis<sup>23</sup> is advantageous in evaluating the net glucose uptake by the brain given the simplicity of the linear regression method when separate information on the transport of FDG to the cellular compartment and its phosphorylation are not necessary. The temporal range examined was fixed between 5 and 27 min, similar to previously published procedures in mice.<sup>25,27</sup> The first few minutes are in fact influenced by equilibration between plasma and tissue FDG, while the last time point included was set to be before 30 min in order to minimize the influence of  $k^*_4$  (dephosphorylation of FDG-6P). FDG-6P reaches typically a plateau 20 min after FDG bolus injection, resulting in a non-negligible effect of dephosphorylation mostly between 30 min and the end of the experiments.<sup>25–27</sup> The effect of a non-negligible dephosphatase activity was discernible from the decline of the Patlak curve in the four time points corresponding to 30 to 50 min (Figure 5(a)).

Linear relationships were established in the aforementioned time frames as justified from R<sup>2</sup> values for each linear fit (0.92–0.99). Reported values and their variability for CMR<sub>glc</sub> in the brain were comparable to other FDG PET studies in mice under isoflurane.<sup>26,27,38,39</sup>

The value of CMR<sub>glc(ox)</sub> derived from the amino acids turnover using <sup>13</sup>C MRS ( $0.38 \pm 0.02 \mu\text{mol/g/min}$ ) is comparable to CMR<sub>glc</sub> quantified from PET experiments. However, a slightly higher glucose metabolism measured by <sup>18</sup>FDG PET is consistent, given that glucose can be in part metabolized by glycolysis to lactate and to a smaller extent to glycogen (<sup>18</sup>FDG PET measures CMR<sub>glc(total)</sub>).

For the present study, we conclude that cerebral brain metabolism can be assessed in vivo in mice with

direct <sup>13</sup>C MR spectroscopy at 14.1 Tesla. Given the high spectral quality obtained in the chosen volume of detection (112  $\mu\text{L}$ ), we expect that sufficient SNR could be obtained in the near future in volumes as small as 60  $\mu\text{L}$  for the detection of C4, C3, and C2 resonances of Glu and Gln, giving access to the detection of regional glucose metabolism in astrocytes and neurons. The FE time courses available from those labeled metabolites allowed us for the first time to obtain a complete two-compartmental description of brain energy metabolism in mice.

### **Funding**

The author(s) disclosed receipt of the following financial support for the research, authorship, and/or publication of this article: This work was supported by Centre d'Imagerie BioMédicale (CIBM) of the UNIL, UNIGE, HUG, CHUV, and EPFL, the Leenaards, Jeantet Foundations and Grant FP7-PEOPLE-2010-ITN-264780.

### **Declaration of conflicting interests**

The author(s) declared no potential conflicts of interest with respect to the research, authorship, and/or publication of this article.

### **Authors' contributions**

Marta Lai: Conception of the experimental designs, acquisition of in vivo <sup>13</sup>C MRS data, experiments, and preliminary studies. Contribution to post-processing, data analysis, and interpretation of experiments. Drafting of the manuscript and figures. Critical manuscript revising. Approval of the manuscript final version.

Bernard Lanz: Conception of the experimental designs, acquisition of in vivo <sup>13</sup>C MRS data, experiments, and preliminary studies. Design and realization of the home-built <sup>13</sup>C coil. Adaptation/extension of mathematical modeling fitting code. Contribution to post-processing, data analysis, and interpretation of experiments. Critical manuscript revision. Approval of the manuscript final version.

Carole Poiry-Yamate: Conception of the experimental <sup>18</sup>FDG PET protocol design, performed <sup>18</sup>FDG PET scans, post-processing, data analysis, and data interpretation. Critical manuscript revision. Approval of the manuscript final version.

Jackeline F. Romero: Animal technical support during acquisition of in vivo <sup>13</sup>C MRS data and preliminary studies. Animal monitoring before and during experiments. Manuscript revising. Approval of the manuscript final version.

Corina M Berset: Animal technical support involving tail vein catheterization of mice planned for non-invasive <sup>18</sup>FDG PET. Animal monitoring before and during experiments. Manuscript revising. Approval of the manuscript final version.

Cristina Cudalbu: Conception of the experimental designs and contribution to preliminary studies. Contribution to data analysis and interpretation. Critical manuscript revising. Approval of the manuscript final version.

Rolf Gruetter: Conception of the experimental designs. Conception of metabolic modeling scheme. Data analysis and interpretation. Critical manuscript revising. Approval of the manuscript final version.

### Supplementary material

Supplementary material for this paper can be found at the journal website: <http://journals.sagepub.com/home/jcb>

### References

- Gruetter R, Adriany G, Choi I-Y, et al. Localized in vivo  $^{13}\text{C}$  NMR spectroscopy of the brain. *NMR Biomed* 2003; 16: 313–338.
- Rothman DL, De Feyter HM, de Graaf RA, et al.  $^{13}\text{C}$  MRS studies of neuroenergetics and neurotransmitter cycling in humans. *NMR Biomed* 2011; 24: 943–957.
- Lanz B, Gruetter R and Duarte JMN. Metabolic flux and compartmentation analysis in the brain in vivo. *Front Endocrinol* 2013; 4: 156.
- Gruetter R, Seaquist ER and Ugurbil K. A mathematical model of compartmentalized neurotransmitter metabolism in the human brain. *Am J Physiol Endocrinol Metab* 2001; 281: E100–E112.
- Sibson NR, Mason GF, Shen J, et al. In vivo  $^{13}\text{C}$  NMR measurement of neurotransmitter glutamate cycling, anaplerosis and TCA cycle flux in rat brain during  $[2-^{13}\text{C}]$ glucose infusion. *J Neurochem* 2001; 76: 975–989.
- Duarte JMN, Lanz B and Gruetter R. Compartmentalized cerebral metabolism of  $[1,6-^{13}\text{C}]$ glucose determined by in vivo  $^{13}\text{C}$  NMR spectroscopy at 14.1 T. *Front Neuroenergetics* 2011; 3: 3.
- van Eijsden P, Behar KL, Mason GF, et al. In vivo neurochemical profiling of rat brain by  $^1\text{H}$ - $[^{13}\text{C}]$  NMR spectroscopy. Cerebral energetics and glutamatergic/GABAergic neurotransmission. *J Neurochem* 2010; 112: 24–33.
- Lanz B, Xin L, Millet P, et al. In vivo quantification of neuro-glial metabolism and glial glutamate concentration using  $^1\text{H}$ - $[^{13}\text{C}]$  MRS at 14.1 T. *J Neurochem* 2014; 128: 125–139.
- Henry P-G, Tkáč I and Gruetter R.  $^1\text{H}$ -localized broadband  $^{13}\text{C}$  NMR spectroscopy of the rat brain in vivo at 9.4 T. *Magn Reson Med* 2003; 50: 684–692.
- Graaf RA de, Mason GF, Patel AB, et al. Regional glucose metabolism and glutamatergic neurotransmission in rat brain in vivo. *PNAS* 2004; 101: 12700–12705.
- Xin L, Lanz B, Lei H, et al. Assessment of metabolic fluxes in the mouse brain in vivo using  $^1\text{H}$ - $[^{13}\text{C}]$  NMR spectroscopy at 14.1 Tesla. *J Cereb Blood Flow Metab* 2015; 35: 759–765.
- Shestov AA, Valette J, Ugurbil K, et al. On the reliability of  $^{13}\text{C}$  metabolic modeling with two-compartment neuronal-glial models. *J Neurosci Res* 2007; 85: 3294–3303.
- Nabuurs CL, Klomp DW, Veltien A, et al. Localized sensitivity enhanced in vivo  $^{13}\text{C}$  MRS to detect glucose metabolism in the mouse brain. *Magn Reson Med* 2008; 59: 626–630.
- Patel AB, Graaf RA de, Mason GF, et al. The contribution of GABA to glutamate/glutamine cycling and energy metabolism in the rat cortex in vivo. *PNAS* 2005; 102: 5588–5593.
- Choi I-Y, Lei H and Gruetter R. Effect of deep pentobarbital anesthesia on neurotransmitter metabolism in vivo: on the correlation of total glucose consumption with glutamatergic action. *J Cereb Blood Flow Metab* 2002; 22: 1343–1351.
- Gruetter R and Tkáč I. Field mapping without reference scan using asymmetric echo-planar techniques. *Magn Reson Med* 2000; 43: 319–323.
- Mlynárik V, Gambarota G, Frenkel H, et al. Localized short-echo-time proton MR spectroscopy with full signal-intensity acquisition. *Magn Reson Med* 2006; 56: 965–970.
- Provencher SW. Automatic quantitation of localized in vivo  $^1\text{H}$  spectra with LCModel. *NMR Biomed* 2001; 14: 260–264.
- Lanz B, Poitry-Yamate C and Gruetter R. Image-derived input function from the vena cava for  $^{18}\text{F}$ -FDG PET studies in rats and mice. *J Nucl Med* 2014; 55: 1380–1388.
- Shank RP, Bennett GS, Freytag SO, et al. Pyruvate carboxylase: an astrocyte-specific enzyme implicated in the replenishment of amino acid neurotransmitter pools. *Brain Res* 1985; 329: 364–367.
- Martinez-Hernandez A, Bell KP and Norenberg MD. Glutamine synthetase: glial localization in brain. *Science* 1977; 195: 1356–1358.
- Canavos GC. A Monte Carlo investigation of experimental data requirements for fitting polynomial functions, <http://ntrs.nasa.gov/search.jsp?R=19740018957> (1974, accessed 27 September 2016).
- Patlak CS, Blasberg RG and Fenstermacher JD. Graphical evaluation of blood-to-brain transfer constants from multiple-time uptake data. *J Cereb Blood Flow Metab* 1983; 3: 1–7.
- Toyama H, Ichise M, Liow J-S, et al. Absolute quantification of regional cerebral glucose utilization in mice by  $^{18}\text{F}$ -FDG small animal PET scanning and  $^2\text{-}^{14}\text{C}$ -DG autoradiography. *J Nucl Med* 2004; 45: 1398–1405.
- Wu H-M, Sui G, Lee C-C, et al. In vivo quantitation of glucose metabolism in mice using small-animal PET and a microfluidic device. *J Nucl Med* 2007; 48: 837–845.
- Kreissl MC, Stout DB, Wong K-P, et al. Influence of dietary state and insulin on myocardial, skeletal muscle and brain  $[^{18}\text{F}]$ -fluorodeoxyglucose kinetics in mice. *EJNMMI Res* 2011; 1: 8.
- Yu AS, Lin H-D, Huang S-C, et al. Quantification of cerebral glucose metabolic rate in mice using  $^{18}\text{F}$ -FDG and small-animal PET. *J Nucl Med* 2009; 50: 966–973.
- Patel AB, de Graaf RA, Rothman DL, et al. Evaluation of cerebral acetate transport and metabolic rates in the rat brain in vivo using  $^1\text{H}$ - $[^{13}\text{C}]$ -NMR. *J Cereb Blood Flow Metab* 2010; 30: 1200–1213.
- de Graaf RA, Brown PB, Mason GF, et al. Detection of  $[1,6-^{13}\text{C}_2]$ -glucose metabolism in rat brain by in vivo  $^1\text{H}$ - $[^{13}\text{C}]$ -NMR spectroscopy. *Magn Reson Med* 2003; 49: 37–46.
- Tiwari V, Ambadipudi S and Patel AB. Glutamatergic and GABAergic TCA cycle and neurotransmitter cycling

- fluxes in different regions of mouse brain. *J Cereb Blood Flow Metab* 2013; 33: 1523–1531.
31. Jeffrey FM, Marin-Valencia I, Good LB, et al. Modeling of brain metabolism and pyruvate compartmentation using (13)C NMR in vivo: caution required. *J Cereb Blood Flow Metab* 2013; 33: 1160–1167.
  32. Tkáč I, Henry P-G, Andersen P, et al. Highly resolved in vivo 1H NMR spectroscopy of the mouse brain at 9.4T. *Magn Reson Med* 2004; 52: 478–484.
  33. Ori C, Dam M, Pizzolato G, et al. Effects of isoflurane anesthesia on local cerebral glucose utilization in the rat. *Anesthesiology* 1986; 65: 152–156.
  34. Alkire MT, Haier RJ, Shah NK, et al. Positron emission tomography study of regional cerebral metabolism in humans during isoflurane anesthesia. *Anesthesiology* 1997; 86: 549–557.
  35. Tkáč I, Rao R, Georgieff MK, et al. Developmental and regional changes in the neurochemical profile of the rat brain determined by in vivo 1H NMR spectroscopy. *Magn Reson Med* 2003; 50: 24–32.
  36. Boretius S, Tammer R, Michaelis T, et al. Halogenated volatile anesthetics alter brain metabolism as revealed by proton magnetic resonance spectroscopy of mice in vivo. *Neuroimage* 2013; 69: 244–255.
  37. Horn T and Klein J. Lactate levels in the brain are elevated upon exposure to volatile anesthetics: a microdialysis study. *Neurochem Int* 2010; 57: 940–947.
  38. Alf MF, Wyss MT, Buck A, et al. Quantification of brain glucose metabolism by 18F-FDG PET with real-time arterial and image-derived input function in mice. *J Nucl Med* 2013; 54: 132–138.
  39. Mizuma H, Shukuri M, Hayashi T, et al. Establishment of in vivo brain imaging method in conscious mice. *J Nucl Med* 2010; 51: 1068–1075.
  40. Sibson NR, Dhankhar A, Mason GF, et al. In vivo 13C NMR measurements of cerebral glutamine synthesis as evidence for glutamate–glutamine cycling. *PNAS* 1997; 94: 2699–2704.